J Mater Sci: Mater Electron (2026) 37:1212

Flexible PET-based resistive tactile sensors via a hybrid fabrication approach using reduced graphene oxide/silver nanoparticle nanocomposite electrodes and graphene piezoresistive layer

Muhammad Izzuddin Mohamad Azhar[1], Aliza Aini Md Ralib[1,*], Nor Hidayati Diyana Nordin[2], Syed Muhammad Hafiz Syed Mohd Jaafar[3], Shafarina Azlinda Ahmad Kamal[4], Nurul Hazierah Kamaruddin[5], and Aiman Sajidah Abd Aziz[5]

[1] *VLSI-MEMS Research Unit, Department of Electrical and Computer Engineering, Kulliyyah of Engineering, International Islamic University Malaysia, Jalan Gombak, 53100 Kuala Lumpur, Malaysia*
[2] *Department of Mechatronics Engineering, Kulliyyah of Engineering, International Islamic University Malaysia, Jalan Gombak, 53100 Kuala Lumpur, Malaysia*
[3] *Centre of Innovative Nanostructure and Nanodevices (COINN), Universiti Teknologi PETRONAS, Seri Iskandar, 32610 Ipoh, Perak, Malaysia*
[4] *Low Dimensional Materials Research Centre, Department of Physics, Faculty of Science, University of Malaya, 50603 Kuala Lumpur, Malaysia*
[5] *Semiconductor R&D, MIMOS Berhad, Jalan Inovasi 3, Taman Teknologi Malaysia, 57000 Wilayah Persekutuan Kuala Lumpur, Malaysia*

Received: 9 March 2026
Accepted: 16 May 2026

ABSTRACT

Precise measurement of force and pressure plays a vital role in human motion monitoring where it widely used in rehabilitation to track grip strength by measuring force distribution generated during movement. Flexible commercial resistive force sensor or so called force sensitive resistors (FSRs) are widely used in wearable electronics for detecting force changes associated with human motion. While commercial FSRs are commonly employed, it lacks adaptability, flexibility and ergonomic fit required in rehabilitation settings. Personalized and custom-made resistive sensors provide tailored sensing range, sensitivity and flexibility to facilitate personalized therapy. Hence, this work explores the new technique for developing a flexible PET-based resistive tactile sensor using a hybrid fabrication approach. The developed sensor consists of the interdigitated electrode, piezoresistive layer, and the gap spacer. The reduced graphene oxide/silver nanoparticle nanocomposite electrodes layer was fabricated using inkjet printing, while the graphene piezoresistive layer was fabricated using stencil printing. The measurement setup consists of dynamic mechanical analysis (DMA) system to analyze the sensing range, sensitivity, response and recovery time, and stability.

Address correspondence to E-mail: alizaaini@iium.edu.my

https://doi.org/10.1007/s10854-026-17553-w
Published online: 29 May 2026

Measurement result shows a nonlinear response similar to the commercial FSR. The fabricated PET-based resistive tactile sensor achieved fractional change of resistance of 0.35 and reaching saturated resistance at 35 kPa. Low response time and recovery time was also recorded at 164.04 ms and 161.54 ms, respectively. The custom PET-based resistive tactile sensor demonstrated stable performance with minimal variation of output signal when subjected to a constant displacement and load over 400 load cycles at a frequency of 1 Hz. The sensor was tested in a system to detect gripping action by sensing muscle contraction forces from 3 upper forearm muscle groups. Hence, the proposed flexible PET-based resistive tactile sensor using inkjet printable rGO/AgNP nanocomposites conductive ink and graphene ink has high potential to be used for wearable pressure sensing applications.

1 Introduction

The current trend of wearable electronics is that these devices are opting for sensors that are becoming more flexible. While current rigid devices are still able to obtain signals from humans, the rigidity causes them to lack adaptability to various scenarios [1]. The demand for flexibility inside these sensors are increasing in various applications such as health monitoring devices [2–4], soft robotics [5–7], sensors for smart clothes [8, 9], and flexible displays [10, 11]. Specifically, tactile sensors are among the growing areas for flexible electronics. Tactile sensors detect signals from various mechanical stimuli such as force [12, 13], strain [14, 15], and bending [16, 17]. Because of this, the sensors can easily adapt to the scenario for obtaining real-time data through kinetic motion [18]. They can be used in many applications such as muscle activity [19, 20], space exploration [21, 22] and virtual reality gaming [23, 24].

There have been various sensing mechanisms used in tactile sensors, such as piezoresistivity [25–30], piezoelectricity [25–30], and capacitive sensing [25–30]. However, piezoelectric sensing is highly susceptible to temperature, and the mechanism output can slowly drift over time [26, 30]. As for capacitive sensing, the capacitance between two plates in a sensor is susceptible to parasitic capacitance that can affect measurements in practical applications [31, 32]. Hence, current research has explored the fabrication of flexible sensors using the piezoresistive sensing mechanism due to its simple read-out mechanism [26, 30, 33].

There are many types of sensors that have utilized the piezoresistive sensing mechanism such as resistive tactile sensors [12, 34–37], material geometry sensors [34, 37, 38], and MEMS pressure sensors [39, 40]. Resistive tactile sensors are sensors that exhibit a decrease in resistance when force is applied. This is caused by the main electrode component being in contact with the piezoresistive component, forming a conducting path to allow current flow.

Commercial versions of these sensors, also known as Force Sensitive Resistors (FSRs) also use the piezoresistive sensing mechanism. FSRs have been explored in many applications such as force myography [41, 42], posture monitoring [35], and robotic grippers [12]. Although they have been employed in many applications, current commercial FSRs are lacking in adaptability for specific applications. Therefore, a custom-made resistive tactile sensor with simple fabrication process will be highlighted in this work for rapid prototyping and ensure sensor performance is enhanced for wearable tactile sensing applications.

There are various fabrication techniques that can be used to fabricate custom-made resistive tactile sensors such as using microstructure molding [43–45], dip coating [38, 46, 47], and printing techniques [12, 35, 36]. Microstructure molding is an emerging fabrication process that mixes a polymer material with a conductive binder and casted into a microstructured master mold made out of silicon or metal [48]. While microstructure molding provides flexibility in sensor design fabrication, the fabrication process is inefficient for rapid prototyping due to the lack of consistency caused between different batches produced from each master mold. Dip coating is another fabrication method where a polymer material is dipped onto a conductive solution, resulting in a conductive material [49]. While this method is simple, it lacks the flexibility of fabricating various designs due to the process

requiring coating the entire structure into the conductive solution. Printing techniques are chosen for this work as it provides simple and scalable fabrication, while also allowing for various design modifications to produce a high performance resistive tactile sensor.

Printing techniques play an important role in fabricating a printed resistive tactile sensor. It is crucial to determine which type of printing method is suitable the sensor design and geometry can be modified for rapid prototyping processes. Among the printing techniques used for flexible sensors are screen printing [12, 35, 37], 3D printing [7, 50], and inkjet printing [51, 52]. Screen printing is widely used for printed flexible sensors. However, it has limitations including stencil mesh degradation [49], ink wastage from mesh retention [53, 54] and the need for highly viscous ink that make the stencil mesh harder [55], which is also difficult to clean. Hence, inkjet printing was chosen for sensor fabrication in this work as it eliminates the need for physical stencil mesh enables direct digital pattern design [56–58].

Inkjet printing also minimizes material wastage via drop-on-demand (DOD) mechanism where it will only deposit low viscosity ink onto the substrate when needed. [55, 59]. There have also been inkjet-printed resistive tactile sensors recorded from previous works [36, 51, 52]. However, current works use commercial conductive inks that lack modification for specific wearable sensing applications.

Conductive inks are among the common challenges in inkjet printing. This is because not only the conductive inks used to fabricate the sensor demands high electrical performance, but the ink should also possess mechanical stability after the printing process has been completed, to increase the sensor lifetime. There are various conductive inks that have been used to fabricate inkjet-printed pressure sensors. Among them are carbon nanomaterials ink, metal nanomaterials ink, and conductive polymers. Carbon nanomaterials are commonly used in pressure sensors due to the low cost, high chemical stability, and high piezoresistive properties. Commonly used carbon nanomaterials ink are graphene and carbon nanotubes (CNT). Graphene is a carbon nanomaterial that consists of a 2D carbon material nanostructure at an atomic thickness. This causes it to have strong mechanical properties that has high potential in pressure sensing applications. However, graphene is very hydrophobic in nature and may not be feasible to be formulated into a conductive ink. Hence, current research works have focused more on ink based on graphene oxide (GO). GO-based ink requires a reduction process, to ensure it becomes conductive to formed reduced graphene oxide (rGO). rGO, as a derivative of graphene, inherits all its properties to obtain performance similar to pristine graphene. However, the rGO nanostructures contain oxygen groups that can inhibit their electrical properties, and has a lower conductivity compared to pristine graphene.

Hence, the novelty of this work will develop a custom-made contact resistive tactile sensor that consists of an electrode, piezoresistive layer fabricated onto flexible PET-substrates, and the gap spacer. A formulated nanocomposite ink that consists of reduced graphene oxide and silver nanoparticles will be used to fabricate the electrode layer using inkjet printing technique. The proposed nanocomposite ink has the potential to improve the performance of the sensor by combining the flexible properties of reduced graphene oxide (rGO) sheets with the conductive properties of the silver nanoparticles (AgNPs), demonstrating similar conductivity of the printed sensor, at higher values of force.

The organization of the article are as follows. Section 2 discusses on the design concept and the sensing mechanism of the resistive tactile sensor. Section 3 explores the experimental section of the ink formulation, sensor fabrication along with the material characterization of each component along with the measurement setup of the assembled sensor. Section 4 presents the results of the fabricated components of sensor, along with the performance of assembled FSR. Finally, the conclusion and future works were given in Sect. 5.

2 Design concept and sensing mechanism

The resistive tactile sensor fabricated in this work is based on the Shunt Mode Force Sensitive Resistor (FSR 402, Interlink Electronics). The sensor consists of 4 main components which are the 2 substrates, the electrode layer, the piezoresistive layer, and the gap spacer. Firstly, the two substrates are the flexible surfaces that holds the electrode layer and the piezoresistive layer. The electrode layer maintains current flow in the circuit and must be stable when a load of force is applied. The piezoresistive layer helps increase current flow by adding more conducting paths when a force is applied. Lastly, the gap spacer is the component that holds the piezoresistive layer and prevent false

readings of the sensor when there is no force applied. The isometric view and exploded view of the sensor is shown in Fig. 1a and Fig. 1b, respectively, to show the topology and the arrangement of the entire sensor. The sensor has two sections as visualized at the top view in Fig. 1c, where the square area is the sensing area, and the tail extended from the sensing area is for connecting the sensor with the external circuit. Figure 1c also shows the dimensions of width of electrode and gap between electrodes.

The sensing mechanism of the resistive tactile sensor follows a percolation-driven contact resistance sensing mechanism as shown in Fig. 1d. This mechanism follows the working principle mentioned from Weis and Worn [60]. When in the initial state, there will be no conducting paths formed, and resistance will be at its maximum. When a force is applied onto the electrode layer in the pressed state, it increases the conductive pathways thus increase the contacts resistance. The contact between the electrode and

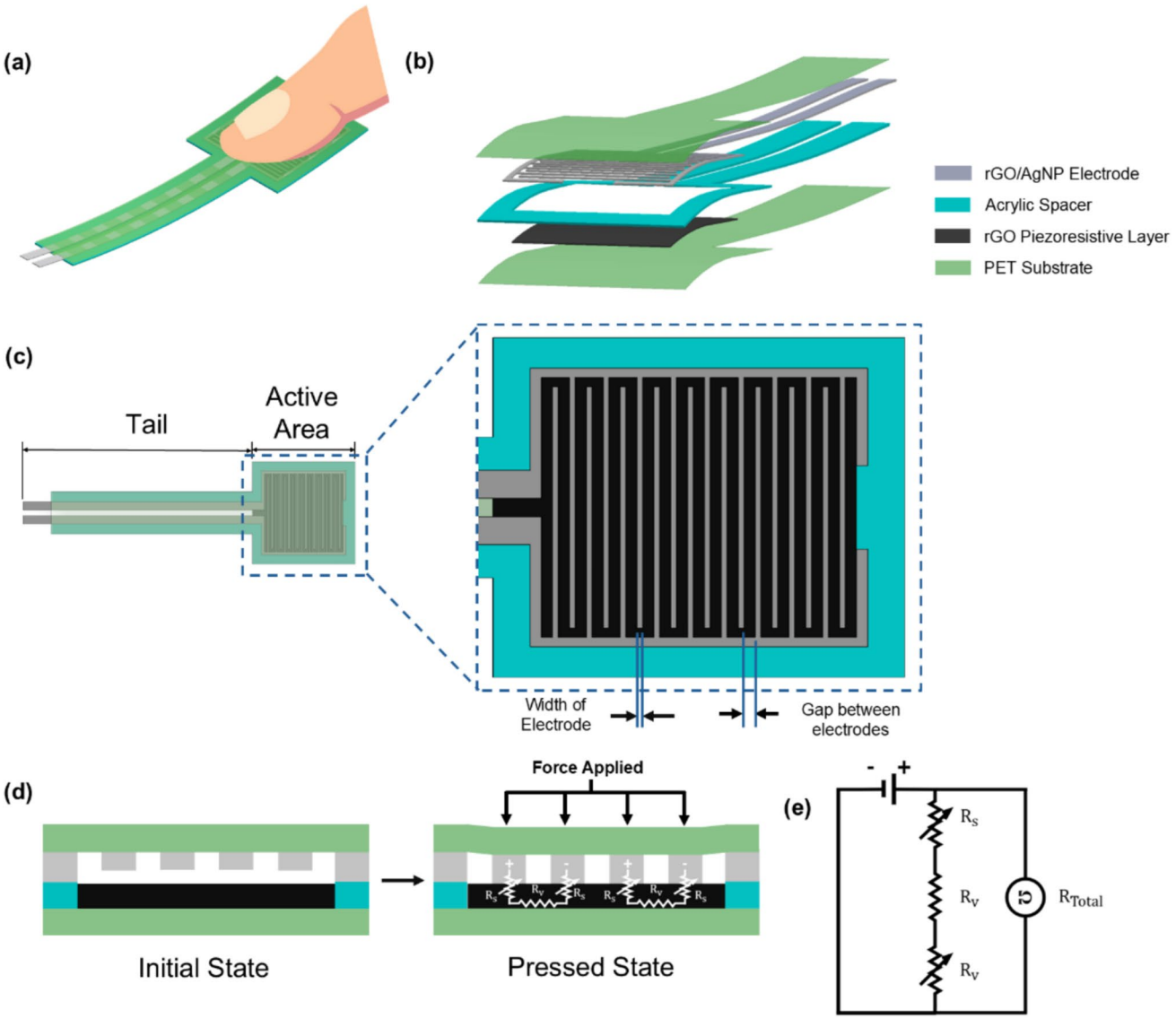

Fig. 1 **a** The isometric view of the flexible PET-based resistive tactile sensor. **b** The exploded view of the sensor, showing the individual components. **c** The top view of the sensor, consisting of the tail and the sensing area. The sensing area is zoomed in to view the width of electrode and gap between electrodes. **d** The cross-section of the sensing area of the sensor, demonstrating the sensing mechanism and resistance path of each pair of electrodes at a pressed state. **e** The equivalent circuit of each pair of contacted electrodes. The total resistance, R_{Total} is measured during the pressed state

piezoresistive layer results in the interface resistance, R_s. When more force is applied, the volume resistance of the piezoresistive layer, R_v, will also decrease due to the changes in geometry of the model [60]. This results in Eq. 1:

$$R_{Total} = 2R_S + R_V \quad (1)$$

From this equation, the equivalent circuit of each pair of electrodes contacting the piezoresistive layer during the pressed state can be summarized in Fig. 1e.

3 Experimental section

3.1 Materials for resistive tactile force sensor fabrication

Polyethylene terephthalate (PET) sheets were purchased online from a local site (Shopee Malaysia) as the flexible substrate for both the electrode layer and the piezoresistive layer. Generally, for the fabrication of the electrode layer, reduced graphene oxide/silver nanoparticles (rGO/AgNPs) nanocomposite ink was synthesized as explained in Sect. 3.2 was used. The piezoresistive layer uses a reduced graphene oxide (rGO) ink (Mi-GraphPrInk, MIMOS Berhad), where the parameters of the ink will be discussed in Sect. 3.3. For the gap spacer, acrylic double-sided tape (Sony G9900) was used, with the adhesive thickness without its backing paper is 0.15 mm.

3.2 Formulation of rGO/AgNP nanocomposite ink

This optimized nanocomposite ink was formulated using the exact reduction method from Ismail et. al. [61]. To prepare the hybrid rGO/AgNPs ink, graphene oxide (GO) was first exfoliated by sonicating and stirring a 1 mg/ml colloid. A mixture of PAA, DEA, and deionized water was added dropwise, followed by silver nitrate ($AgNO_3$) (6.8 M) to serve as the silver source. After stirring for 30 min, the solution was left overnight to allow for AgNP growth. The resulting composite was purified via ethanol washing and centrifugation, then dispersed in deionized water using a nano-premixer to achieve a 0.1 g/ml concentration of hybrid rGO/AgNP colloid. Finally, the hybrid colloid was blended with methanol and ethylene glycol for rapid drying and viscosity enhancement, respectively, to form a water-based ink [61].

3.3 Materials for piezoresistive layer fabrication

For the fabrication of the piezoresistive layer, graphene conductive ink (Mi-GraphPrInk, MIMOS Berhad) was used. This ink was formulated with a blend of graphene nanoparticles, and uses PEDOT:PSS as a conductive polymer, and binder agent. The ink has a particle size of less than 30 nm, viscosity of approximately 3.8 cP, and a sheet resistance range from 0.10 to 0.25 Ω/sq [62]. The ink has been tested to be compatible with the Dimatix DMP Series materials inkjet printer [62].

3.4 Design parameters of sensor components

Figure S1 shows all the dimensions of the individual components of the FSR. For the substrate in Fig. S1a, the sensing area dimensions were 18.30 mm × 18.30 mm. The tail was extended from the center of the sensing area, with a length of 35.80 mm. The tail also has a length of 7.30 mm. For the electrode Fig. S1b, the sensing area design is a pair of interdigitated electrodes, and each electrode has a tail of length 42.45 mm, which is longer than the substrate tail length. This is for the electrode pair to be crimped with extra legs to ensure easier connectivity with an external circuit. For the sensing area of the electrode in Fig. S1c, the area dimensions were 15.00 mm × 15.00 mm. The width for each electrode was 0.25 mm, while the gap between the electrodes were 0.50 mm. The ratio between electrode width and gap between electrodes have been optimized in a previous finite element simulation work [63]. This was done to ensure that the sensor electrode will contact the piezoresistive layer evenly, ensuring a lower resistance at instantaneous force [63]. Both electrodes were separated at the tail by 1.00 mm gap width. For the piezoresistive layer in Fig. S1d, the area dimensions were 14.00 mm × 14.00 mm. The gap spacer in Fig. S1e, the outer dimensions of the sensing area were 18.30 mm × 18.30 mm, while the inner dimensions were 14.00 mm × 14.00 mm. The inner dimensions of the gap spacer were similar to the dimensions of the piezoresistive layer to ensure that the gap spacer will hold the shape of the piezoresistive layer as the graphene ink dries. This also ensures the thickness of the piezoresistive layer remains constant with the gap spacer thickness during its fabrication.

3.5 Fabrication process of resistive tactile sensor

The PET sheet was cleaned using isopropyl alcohol (IPA) and wiped with a dry cloth. The design of the electrode layer (Layer 1) was loaded on the onto the Dimatix DMP software as a .dxf file. Using the formulated rGO/AgNP ink, the electrode layer was printed using a materials inkjet printer (PiXDRO LP50, SUSS Microtec). The optimum droplet printed was driven by an input waveform with an amplitude of 25–35 V across frequencies ranging from 1 kHz, ranged from 5 to 6 m/s using a Dimatix Samba printhead. Using the temperature of the inkjet printer, which is 40 °C, the printed ink will be dried concurrently when the ink is printed onto the substrate. The optimization of number of printing layers has been reported in previous work [61]. As the number of printed layers increases, the electrode becomes thicker and structurally more complex, which elevates stress concentrations at the layer interfaces and consequently increases the possibility of microcrack formation. Hence, one layer of formulated rGO/AgNP nanocomposite ink was printed onto the PET substrate for this work.

For Layer 2, the gap spacer and piezoresistive layer fabrication in Fig. 2b, another PET sheet was placed on a cutting board. Next, a sheet of double-sided tape was placed onto the PET for cutting using a cutting machine (Cameo 4, Silhouette Studio). The design parameters of the gap spacer were uploaded to the Silhouette Studio software as a .dxf file. Inside the cutting machine software, there were two parameters that was manipulated which were the force, speed and number of passes. The force setting of the cutter was set to 6, the speed was set to 20 mm/s, and number of passes was set to 2. This is to ensure the excess tape can be removed easily from the PET substrate, while retaining the cut shape. Then, the setting data was sent

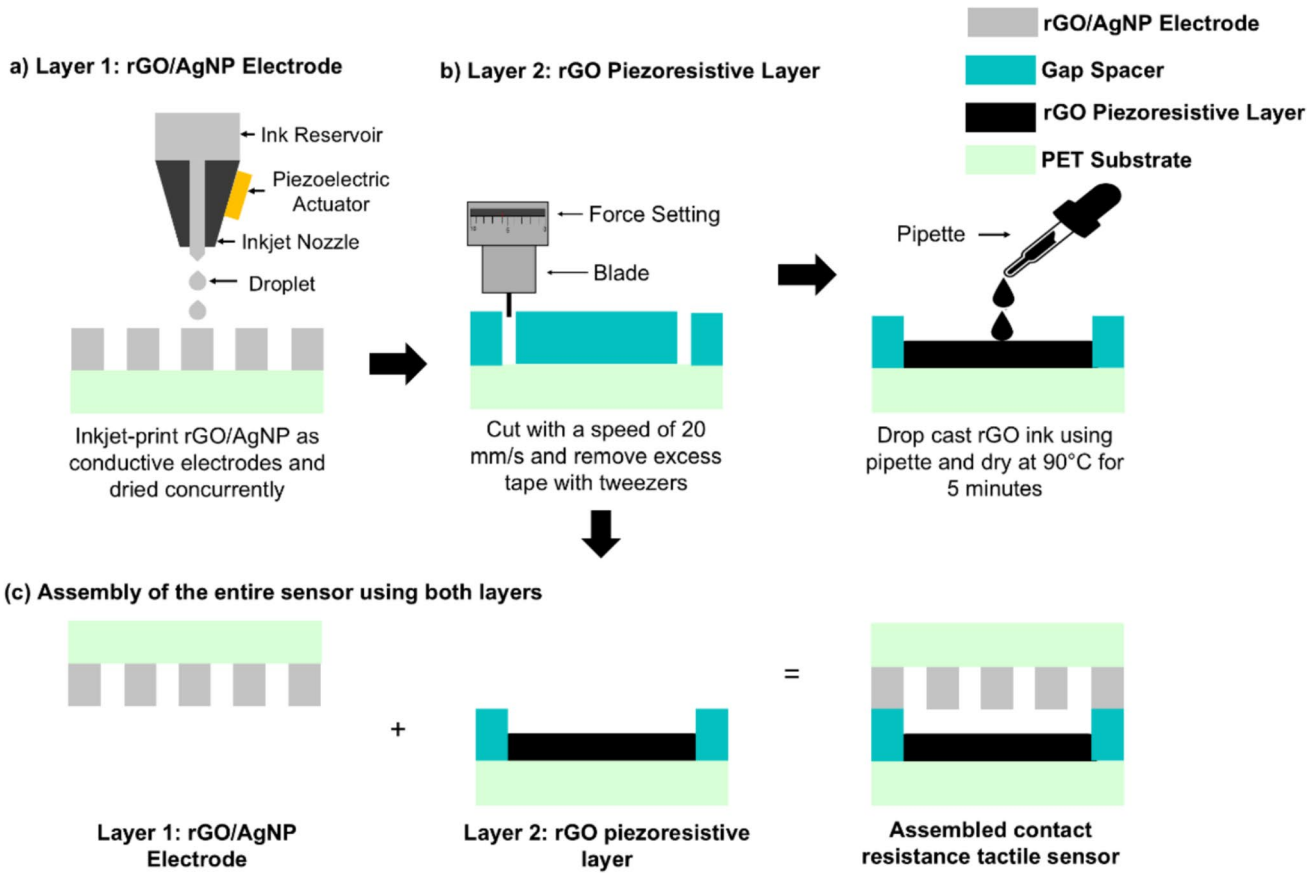

Fig. 2 Fabrication of resistive tactile sensor that consists of 2 layers **a** Layer 1: Inkjet-printed rGO/AgNP as electrode layer on PET substrate, **b** Layer 2: Drop cast rGO ink using pipette on stencil mold prepared using stencil printing and dried for 5 min. **c** Assembly of the entire sensor

to the machine to cut the double-sided tape using the blade into the gap spacer design. Finally, the excess tape surrounding the gap spacer was gently removed using tweezers to obtain the shape before piezoresistive layer fabrication.

Next, for the piezoresistive layer fabrication, the rGO ink from Sect. 3.2 was heated in a beaker under a hot plate. A pipette was used to eject the ink from the beaker at a volume of 50 μL. The ink was drop casted onto the gap spacer area until it is completely filled. The piezoresistive layer was dried at approximately 90 °C for 5 min.

Finally, the assembly of the resistive tactile sensor was done by rotating the electrode layer to face the piezoresistive layer. The release paper of the gap spacer was removed to reveal the adhesive. Then, the electrode layer was aligned and shunted toward the gap spacer and to ensure that all electrodes are perpendicular to the active area of the sensor. Finally, the sensor was crimped as a connector to the external circuit. The summary of the assembly of the sensor was shown in Fig. 2c.

3.6 Material characterization

To obtain the surface morphology of the dried rGO/AgNP electrode, scanning electron microscope (SEM) (JSM-IT100, JEOL), was used. The tail of the electrode was cut into individual 10 mm × 4 mm pieces as samples to be analyzed underneath SEM. Another form of analysis was done using a digital microscope (AM4115ZTL, Dino-Lite Edge) to compare the printed electrode, piezoresistive layer, and gap spacer to the proposed design in Sect. 3.2. This comparison will determine the percentage error of the printed patterns compared to the proposed design. The piezoresistive layer material will be analyzed using Raman spectroscopy (inVia, Renishaw) to verify the Raman shift of the rGO nanoparticles, using a laser power of 10%, and a wavelength of 789 nm. Finally, the sheet resistance of each material was measured using a four-point probe tester (M-3, Suzhou Jingge Electronic).

3.7 Measurement setup

To obtain the measurement of the PET-based resistive tactile sensor, dynamic mechanical analysis (DMA) process was used. The process is visualized in Fig. 3. The Resistive tactile sensor was attached onto the 22N load cell placed on the bottom part of the DMA device (Electroforce 3200, TA Instruments). The sensor was brought close to the optical displacement sensor placed at the top part of the device. The sensor went through a displacement test, where the displacement sensor moves toward the sensor according to the set displacement value in the WinTest software. At the same time, the load cell detects the force value applied by the displacement sensor. 4 displacement tests of 0.45 mm, 0.50 mm, 0.55 mm, and 0.60 mm were conducted onto the resistive tactile sensor, along with a stability test with a constant displacement of 0.50 mm applied. The data were transmitted to the device's data acquisition system, where data from the sensor and load cell will be sent to the multimeter (34410A Digital Multimeter, Agilent Technologies) and DMA data acquisition system, respectively. For mechanical load changes in the DMA, WinTest software was used to graphically display the displacement and load output, while the Agilent connectivity software graphically displayed the resistance.

4 Results and discussion

4.1 Characterization results

As mentioned in Sect. 3.5, the resistive tactile sensor was fabricated using inkjet printing rGO/AgNPs nanocomposite ink for electrode, and drop-casting graphene of the piezoresistive layer. The surface morphology of the fabricated materials was analyzed using SEM. Figure 4a shows the resulting morphology of the rGO/AgNP nanocomposites. This image show the smooth and even surface of the crystalline structure. Figure 4b shows the crystalline structure at a higher magnification. This crystalline structure is defined as the silver nanoparticles, while the rGO remained invisible on the surface [61]. This is caused by the 'embedded' base structure where the AgNPs are decorated onto the surface of the rGO sheets.

The relationship between the number of printed layer and the crack formation under bending cycle has been reported previously [61]. As the number of printed layers increases, the electrode becomes thicker and structurally more complex, leading to a higher stress concentrations at the interfaces between layers and consequently making the electrode more prone to microcrack formation [61]. Small cracks were observed

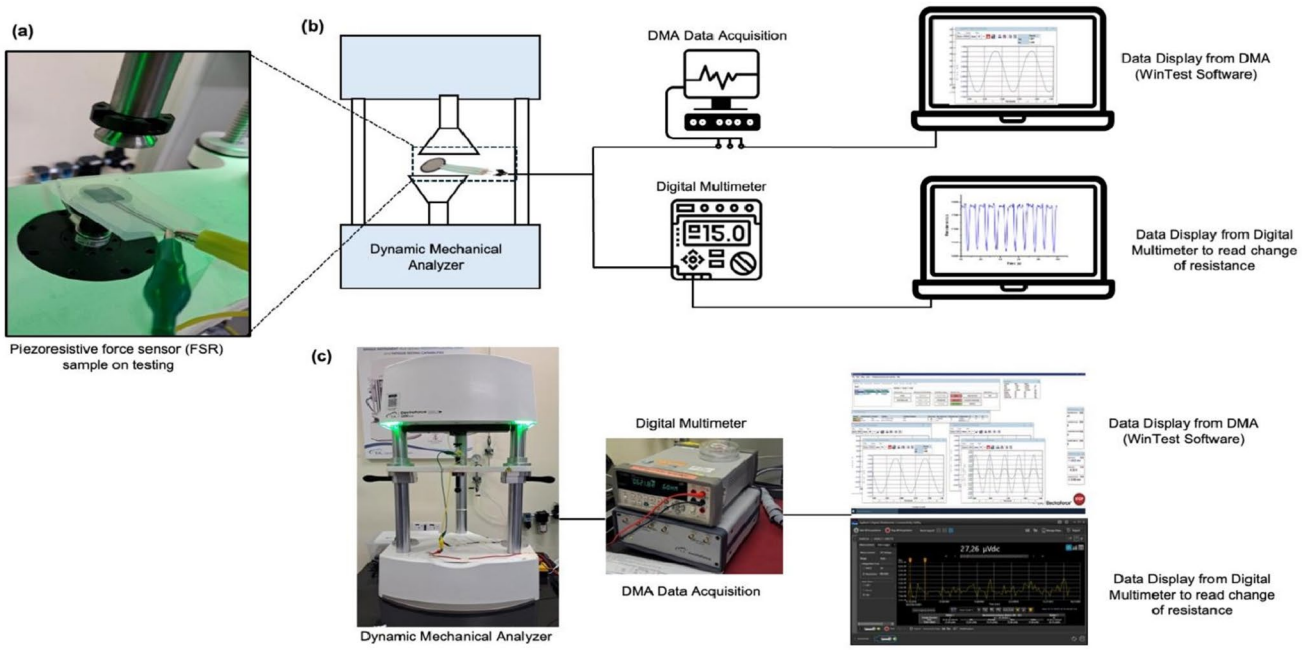

Fig. 3 Measurement setup to obtain the performance parameters of Resistive tactile sensor. **a** Design under test (DUT). **b** Schematic experimental setup that consists of dynamic mechanical analyzer. **c** Actual experimental setup

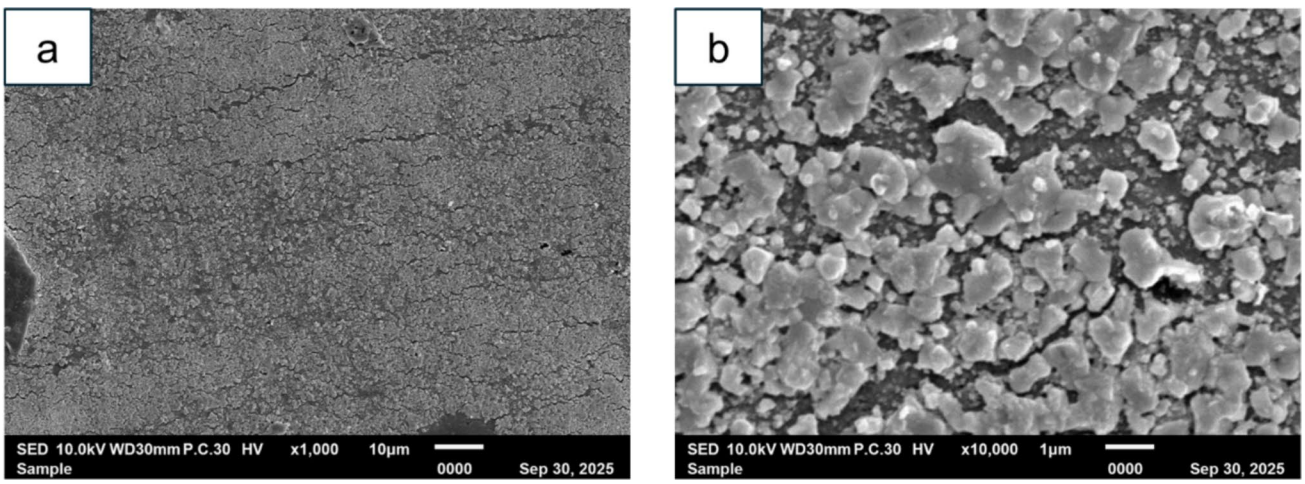

Fig. 4 SEM images of dried rGO/AgNP nanocomposite at **a** × 1000 magnification and **b** × 10,000 magnification

on the surface of the electrode, caused by the drying of the rGO/AgNP nanocomposite ink during the inkjet printing process as shown in Fig. 4a. These cracks cause the embedded AgNPs to branch out and clump together, forming a percolative conductive network with the rGO sheets. Theoretically, under mechanical loading, this conductive network can provide a strong electron flow with the rGO sheets as a flexible scaffold structure, and AgNPs to provide bridges for electrons to flow between the cracks of the rGO sheets, causing an increase in conductivity [64]. Based on this mechanism, only a single layer of formulated rGO/AgNP nanocomposite ink was printed onto the PET substrate in this work. This is because additional layers may result in insufficient sintering of AgNPs which weaken the interfacial bonding between AgNPs and the rGO sheets, and consequently increases the resistance [61].

Figure 5a shows the surface morphology of the drop-casted rGO at × 1000 magnification. Fundamentally, the structure is based on individual rGO sheets. Each of these sheets are stacked against each other, forming a multilayer structure. Figure 5b shows the surface morphology of the rGO at × 10,000 magnification. The images show the nanoparticles appear heavily folded and wrinkled, caused by the reduction process of the graphene oxide (GO) [65]. The reduction process causes the oxygen groups within the GO microstructure to be removed, causing a reduction of surface area within the individual graphene sheets.

Figure 6 shows the resulting Raman spectra for the drop-casted piezoresistive layer using an excitation wavelength of 789 nm. There was one peak that was observed in the drop-casted rGO which was the D band. The D band peaks were centered at 1329.75 cm^{-1}. This proves that the material has defects within the structure, which are the presence of oxygen groups [62].

The fabricated components of the PET-based resistive tactile sensor, which are the inkjet-printed electrode, the drop-casted piezoresistive layer and the gap spacer were all characterized using the same digital microscope. Figure 7a shows the resulting sensor after the assembly process. Figure 7b shows the exploded view of the resulting sensor to show its separate layers. Figure 7c shows a magnified view of the sensing area of the PET-based resistive tactile sensor, particularly to view the electrodes. Figure 7d shows the further magnification of the electrode layer to measure the width of top and bottom inkjet-printed electrodes, and the gap between printed electrodes. The average width of the top and bottom printed electrode was 271.587 μm and 274.313 μm. When comparing with the 250 μm from the CAD design, the margin of error of the top electrode was 8.634%, while the bottom electrode was 9.725%. This printing error is acceptable as the rGO/AgNP ink dried immediately due to the concurrent drying process when depositing the ink onto the substrate. This caused the deposited ink to hold its shape after printing and minimizes bleeding. However, the average gap between electrodes was 482.243 μm. Compared to the CAD design of 500 μm gap, the error was 3.551%. While this error is acceptable, this is caused by the slight shifting of the substrate during the deposition of rGO/AgNP ink in the inkjet printing process.

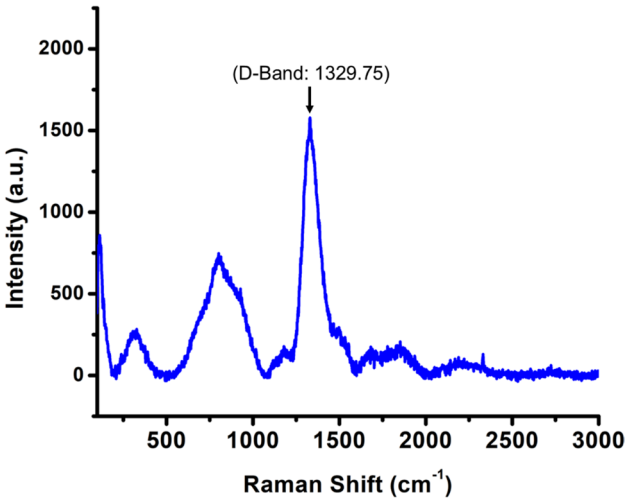

Fig. 6 Raman spectra of rGO piezoresistive layer

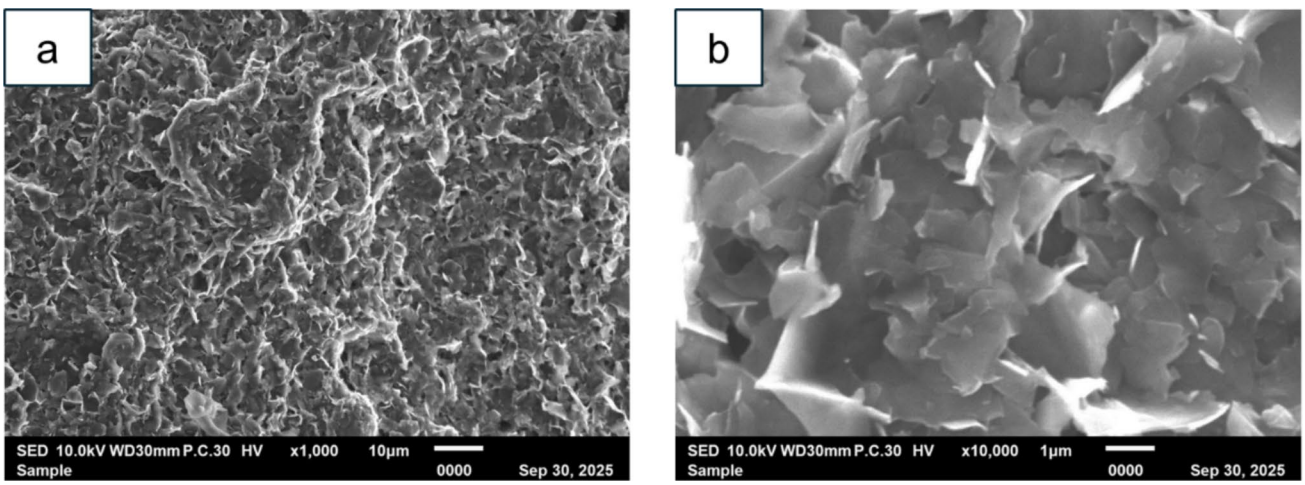

Fig. 5 SEM images of dried rGO nanocomposite at **a** × 1000 magnification and **b** × 10,000 magnification

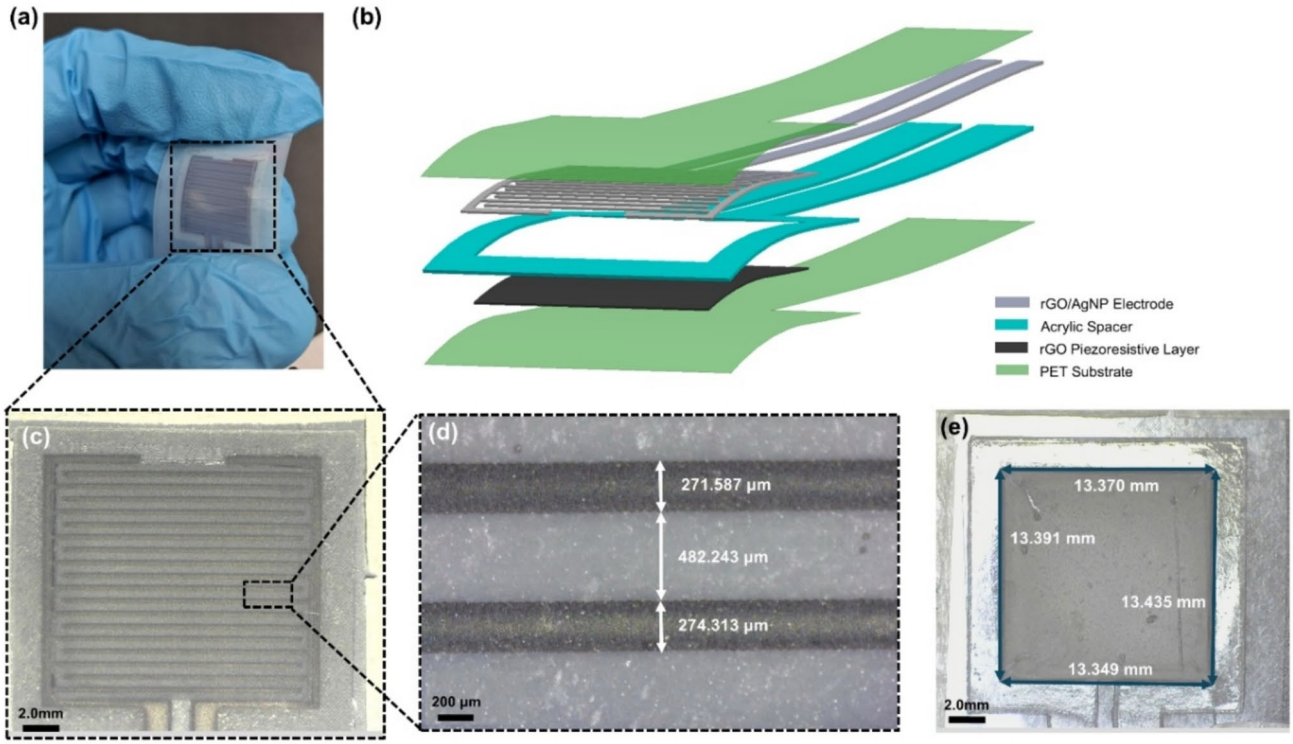

Fig. 7 **a** The resulting fabricated PET-based resistive tactile sensor, held by fingertips as size reference. **b** The exploded view of the sensor components **c** The active area of the PET-based resistive tactile sensor, showing the electrodes with scale bar of 2.0 mm. **d** The magnified view of the top and bottom printed electrodes with scale bar of 200 µm. **e** The resulting gap spacer and piezoresistive layer dimensions with scale bar of 2.0 mm

As for the gap piezoresistive layer characterization in Fig. 7e, the piezoresistive layer showed an average length of 13.360 mm and average width of 13.413 mm. Comparing with the CAD design that has a length of 14 mm and width of 14 mm, the percentage error of the length and width are 4.571% and 4.193%, respectively. This is likely caused by the shrinking of the double-sided tape during the drying process, and lead to the drop-casted piezoresistive layer to also shrink as the solvent evaporates. To mitigate this in future works, the gap spacer may need to increase the dimensions according to the percentage of error to ensure that the shape cut by the cutting machine can be closer to the CAD dimensions after the drying process.

The sheet resistance of each individual components was analyzed using four-point probe and compared using the components from the commercial FSR 402. For reference, the materials of the electrode and the piezoresistive layer from FSR 402 was silver and carbon, respectively. The average value of the sheet resistance of the electrode was measured at 4.22 Ω/sq, while the average value of the of sheet resistance of the piezoresistive layer was measured at 514.78 kΩ/sq.

As for the inkjet-printed rGO/AgNP electrode and drop-casted rGO piezoresistive layer, the sheet resistance of the electrode was measured at 7.89 Ω/sq, while the piezoresistive layer was measured at 465.75 Ω/sq. The inkjet-printed electrode has demonstrated a comparable performance to the commercial electrode, despite being a carbon-based material. This confirms the presence of AgNP to produce more effective conducting paths, causing the resistance to decrease [61]. For the piezoresistive layer, the sheet resistance value was significantly lower than the commercial FSR resistance, which can lead to a lower baseline resistance when the assembled sensor is under load.

4.2 Sensitivity

As mentioned in Sect. 3.4, there were 4 displacement tests that were conducted using DMA, which were 0.45 mm, 0.5 mm, 0.55 mm, and 0.60 mm displacement tests. From each test, 5 loading cycles were extracted.

Figure 8a shows the graph of displacement against time. This graph verifies that the input displacement applied in each test was consistent with every loading cycle. Figure 8b shows the graph of resulting force applied according to the displacement tests, with respect to time. When the optical displacement sensor moves toward the Resistive tactile sensor, the force applied will be detected by the load cell. The graph shows the force that is applied to the Resistive tactile sensor increases when displacement increases, and the consistent displacement in each loading cycle also shows consistent force applied onto the load cell. Similarly, in Fig. 8c, the graph of the resistance of Resistive tactile sensor against time shows a decrease when the load is applied during the displacement test. This verifies the mechanism of the Resistive tactile sensor, where the resistance decreases, when the force increases. This raw data will be used to obtain the sensitivity graph, according to Eq. 2:

$$S = \frac{\Delta R/R_0}{F} \tag{2}$$

where $\Delta R/R_0$ is the fractional change in resistance, ΔR is the change in resistance relative to the initial resistance, R_0 is the initial resistance before the force is applied, and the F is the unit of force in Newton. From the force obtained, the unit of pressure in kilopascal, P, applied onto the sensor will be obtained using Eq. 3:

$$P = \frac{F}{A} \tag{3}$$

where A is the area of the sensing area as mentioned in Sect. 3.4. Figure 8d shows the resulting sensitivity graph in terms of force, while Fig. 8e is the sensitivity graph in terms of pressure. The cause of the significant decrease of the resistive tactile sensor is caused by the contact resistance between the electrode and the piezoresistive layer, where the resistance of contact will decrease when the pressure increases. Additionally, the piezoresistive layer also contributed to the decrease in resistance, where conducting paths were formed between electrode contacts and allowed current flow through the piezoresistive layer, completing the circuit [38].

4.3 Response and recovery time

Response time is defined as the time taken to reach 90% of the stable output value of a sensor when a

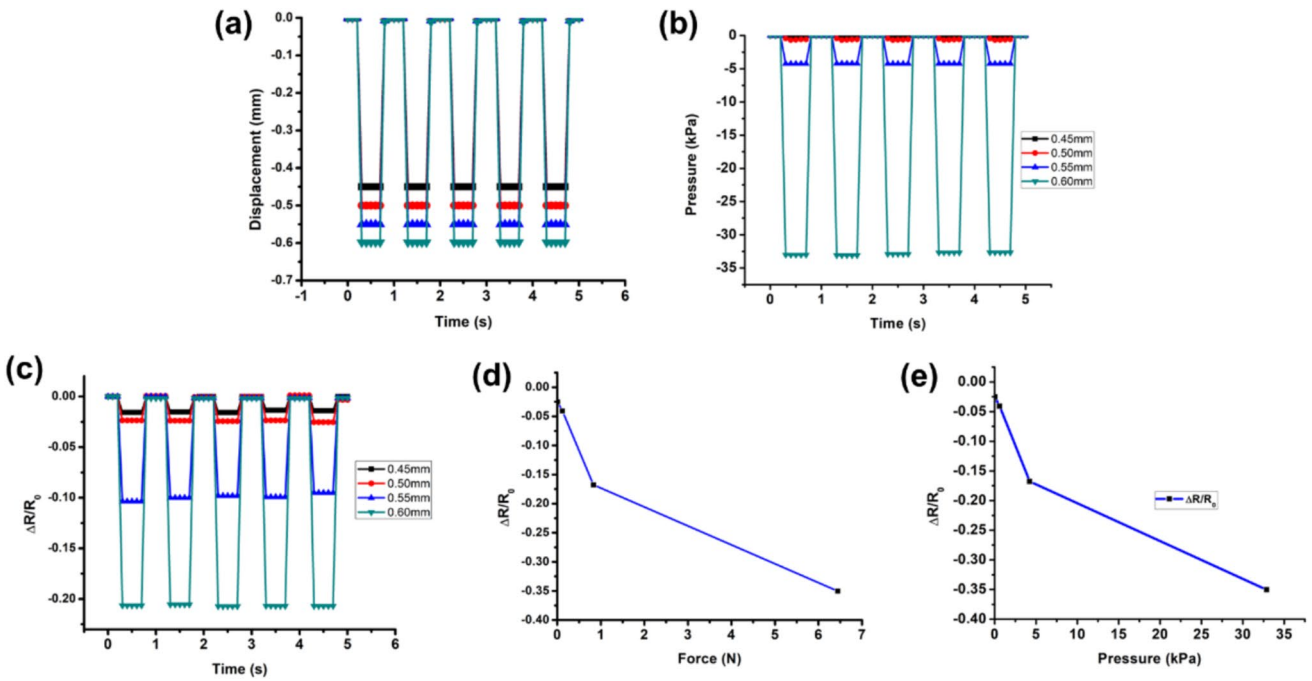

Fig. 8 **a** The graph of displacement against time. **b** The graph of pressure applied against time. **c** The graph of resistance against time. **d** The graph of sensitivity, which is fractional change in resistance against force. **e** The sensitivity graph of fractional change in resistance against pressure

load is applied [27]. Recovery time is defined as the time taken for the sensor to return to 90% of the stable input value, when a load is released. In this context, the PET-based resistive tactile sensor response time is defined as the time taken to reach 90% of the lowest and most stable output of resistive tactile sensor at a certain load. This concept is mirrored by the recovery time, which is the time taken for the Resistive tactile sensor to reach 90% of original resistance value after the load is released. Figure 9 shows the graph of 1 loading cycle of the sensor, obtained from the 0.50 mm displacement test for robustness. The response time of the sensor can be obtained moment the resistance of the sensor drops, which a load is applied at that instance. The response time was 164.04 ms, while the recovery time was 161.54 ms. The response and recovery time obtained during measurement is good for wearable electronics applications as it can quickly detect responses from muscle activity.

4.4 Stability

Stability is defined as the maximum number of loading cycles of a sensor before losing its functionality. In this context, the PET-based resistive tactile sensor stability is defined as the maximum number of loading and unloading cycles needed for the Resistive tactile sensor signal to degrade. In this work, the resistive tactile sensor was tested at the DMA continuously with a displacement test of 0.5 mm, using 400 load cycles at a frequency of 1 Hz. Figure 10a shows the resulting graph produced from the sensor stability test. The resistance changes were consistent throughout the stability test, caused by the conducting paths between the sensor components remained intact. Additionally, there is potential for the sensor to achieve more than 1000 loading cycles. However, the experiment could not be conducted for a longer duration due to limited access time in DMA usage. Figure 10b, c, and d shows the inset of the stability test of periods 110 s–119 s, 200 s–209 s, and 300 s–309 s, respectively. This shows the individual load cycles more clearly, and the sensor output does not degrade during the whole stability test. The primary scope of this study is centered on the novelty of the proposed rGO–Ag nanocomposite ink formulation, hybrid printing-based fabrication approach, and the initial electromechanical validation of the flexible tactile sensor. Within this scope, the demonstrated cyclic stability over 400 cycles is considered sufficient to validate the baseline reliability of the device for low-force wearable sensing applications. Future work will therefore focus on extended lifetime testing and long-term reliability assessment to further support real-world wearable deployment.

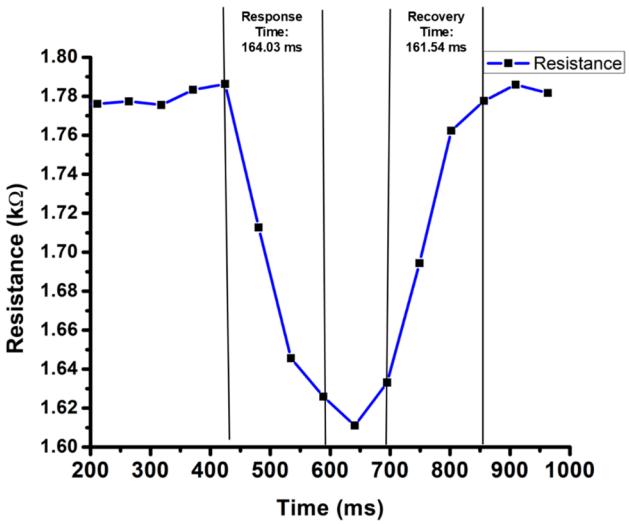

Fig. 9 The graph of 1 resistance loading cycle

For batch to batch consistency, the devices in this study were fabricated following a controlled and repeatable process flow, including consistent ink formulation, printing parameters, and curing conditions to ensure reproducibility. A total of ten devices were fabricated, and an initial quality screening was performed based on contact resistance measurements. Only devices exhibiting variation within 10% were selected for subsequent characterization to minimize batch-induced variability. In addition, quality control was conducted using optical microscopy to assess printing uniformity and feature integrity, while mass measurements before and after curing were used to standardize the active material loading across devices. Multiple devices passing these criteria were tested under identical experimental conditions, and the results exhibited consistent trends in key performance metrics, indicating good device-to-device repeatability. This systematic fabrication and quality assurance approach ensures that the reported data are reliable and representative of the proposed sensor design.

4.5 Performance analysis of resistive tactile sensor with previous works

Using the PET-based resistive tactile sensor's high sensitivity and low detection range, the sensor can be

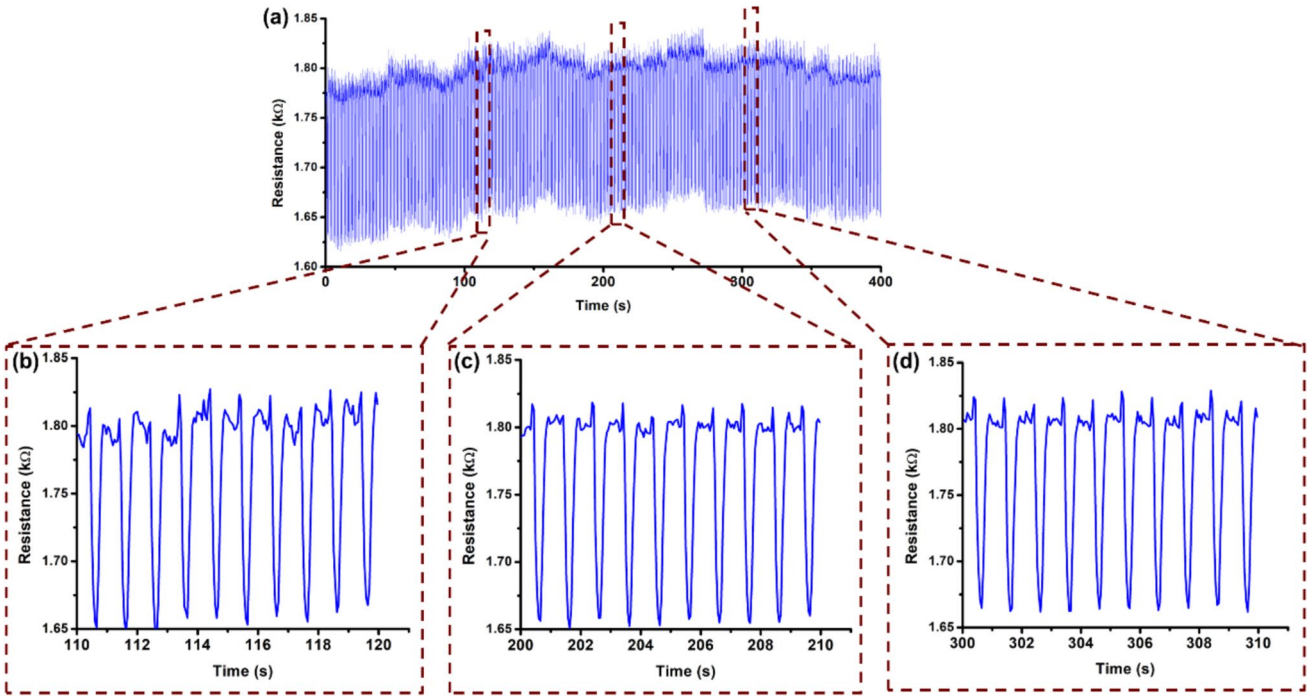

Fig. 10 **a** The resulting graph obtained from the stability test of the sensor. The inset figures show the loading cycles of **b** 110 s – 119 s, **c** 200 s – 209 s, and **d** 300 s – 309 s

a strong candidate for wearable sensing applications. This work presents a simple muscle detection system to detect forearm muscle contraction during hand gripping. Figure 11a shows the resulting experimental setup for muscle contraction detection. Here, the sensor is placed on three different forearm muscle groups, which are the flexor carpi radialis (FCR), flexor digitorium superficialis (FDS), and brachioradialis (BR). This system will detect the change in muscle contractions by using two activities, which the test subject is in the grip position for five seconds, and the release position for 5 s. The hand positions are illustrated in Fig. 11b. The system results are shown in Fig. 11c. During the grip position, the results show a large change in resistance, indicating that all three muscles were contracting and applying pressure onto the sensor. In the release position, all three muscles were relaxed, and the sensor returns to the initial resistance value. From this system, the FCR is shown to have the largest change in resistance, followed by BR and FDS. Notably, in the BR region, there is a slight overshoot during releasing compared to the FCR and FDS, which may be caused by soft tissue oscillation caused by the instant muscle relaxation during the releasing activity. Nevertheless, the sensor was able to obtain a constant resistance change during grip position. Therefore, the sensor is capable of detecting low-force applications related to wearable sensing activities.

As mentioned in Sect. 2, the sensing mechanism of the sensor is when the force increases, the resistance will decrease. This is caused by the force causing a contact between the electrode and the piezoresistive layer. A sensing mechanism comparison using rGO, AgNP, and rGO/AgNP nanocomposite is shown in Fig. 12. For electrode using reduced graphene oxide (rGO) as the material, the resulting structure will retain its shape in its pressed state, due to its high mechanical strength [61]. However, the rGO structure will be less conductive due to the disruption of the pristine lattice structure by the presence of the oxygen groups [66]. This results in a weaker conducting path between the electrode and piezoresistive layer. On the other hand, using a printed silver nanoparticle (AgNPs) electrode shows strong conducting paths formed due to their superior conductivity [26, 30]. However, due to the constant loading and unloading cycles applied onto the electrode, the fabricated electrode will start to form cracks within the printed structure, causing an interruption in the conducting paths [67]. When the rGO was hybridized with AgNP for electrode fabrication (rGO/AgNPs), both the conductivity and flexibility of the individual materials will be retained. This is

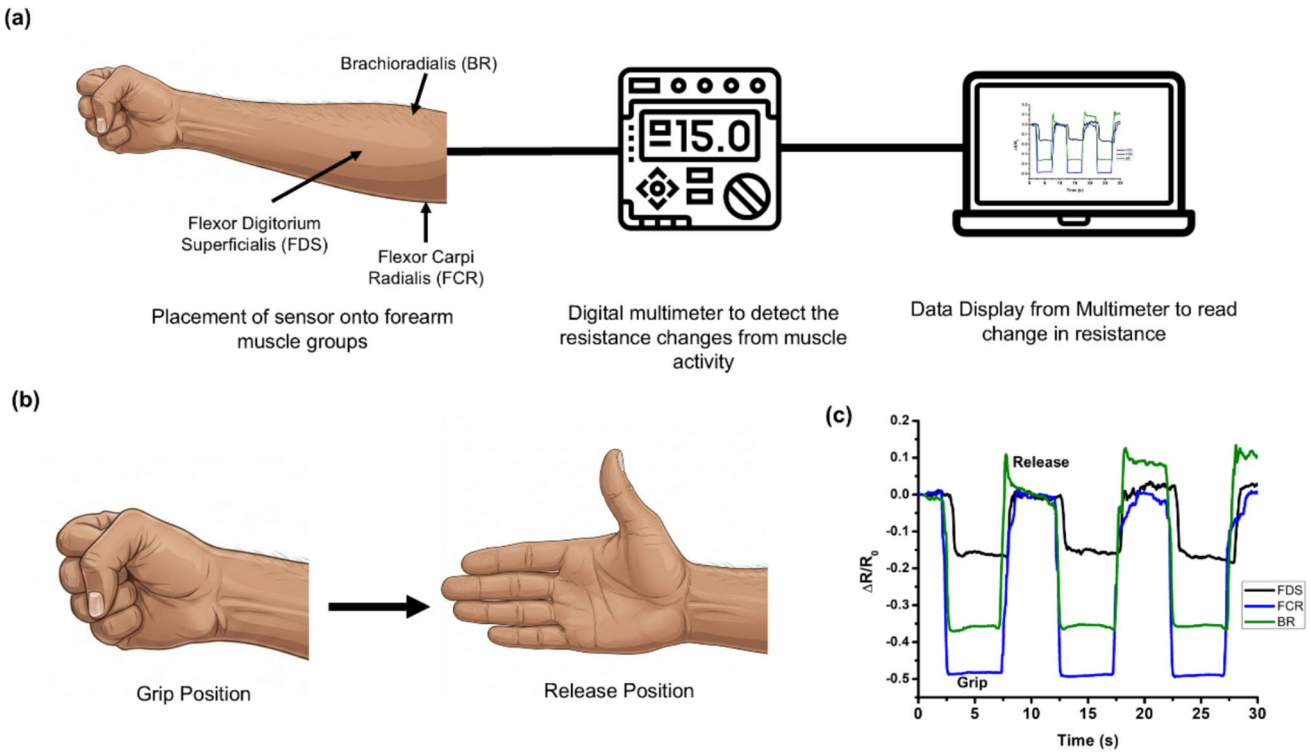

Fig. 11 **a** Experimental setup of resistive tactile sensor for forearm muscle detection. **b** The muscle position detection for detecting muscle contractions. **c** Resulting sensor output from forearm muscle detection

because when the AgNPs are decorated onto the rGO structure, the AgNPs act as a bridge between the rGO sheets, increasing the electrical conductivity [68]. Conversely, the presence of rGO sheets will increase the flexibility of the AgNPs due to their embedded base structure improving bending characteristics without an increase in resistance [69, 70]. Therefore, the usage of hybrid rGO/AgNPs can improve the performance of the sensor in terms of flexibility and conductivity due to their synergistic performance.

The fabricated sensor in this work was compared to other previous works in Table 1. The fabricated sensor has been mainly compared based on the materials of the sensor, fabrication techniques, and performance parameters such as sensitivity, sensing range, response time, and stability. This work has fabricated a sensor that has a maximum fractional change in resistance of 0.35, with a sensing range between 0 and 6.4N. The response and recovery time are 164. 04 ms and 161.54 ms, respectively. The sensor has shown good stability for 100 cycles. The fabricated sensor can potentially be used in wearable sensing applications such as neck palpations [71], hand grip measurement [72], and gait cycle [73]. Hence, the novelty of this work is the usage of the AgNP/rGO nanocomposites on the printing of electrodes for a sensor.

5 Conclusion

In this work, an inkjet-printed resistive tactile sensor was proposed to help improve the flexibility of tactile sensors in wearable electronics. The sensing mechanism of the sensor was introduced, where the sensor was fabricated using an inkjet printing technique for the silver electrode layer and drop casting for the piezoresistive layer. Then, the sensor components were assembled with an acrylic

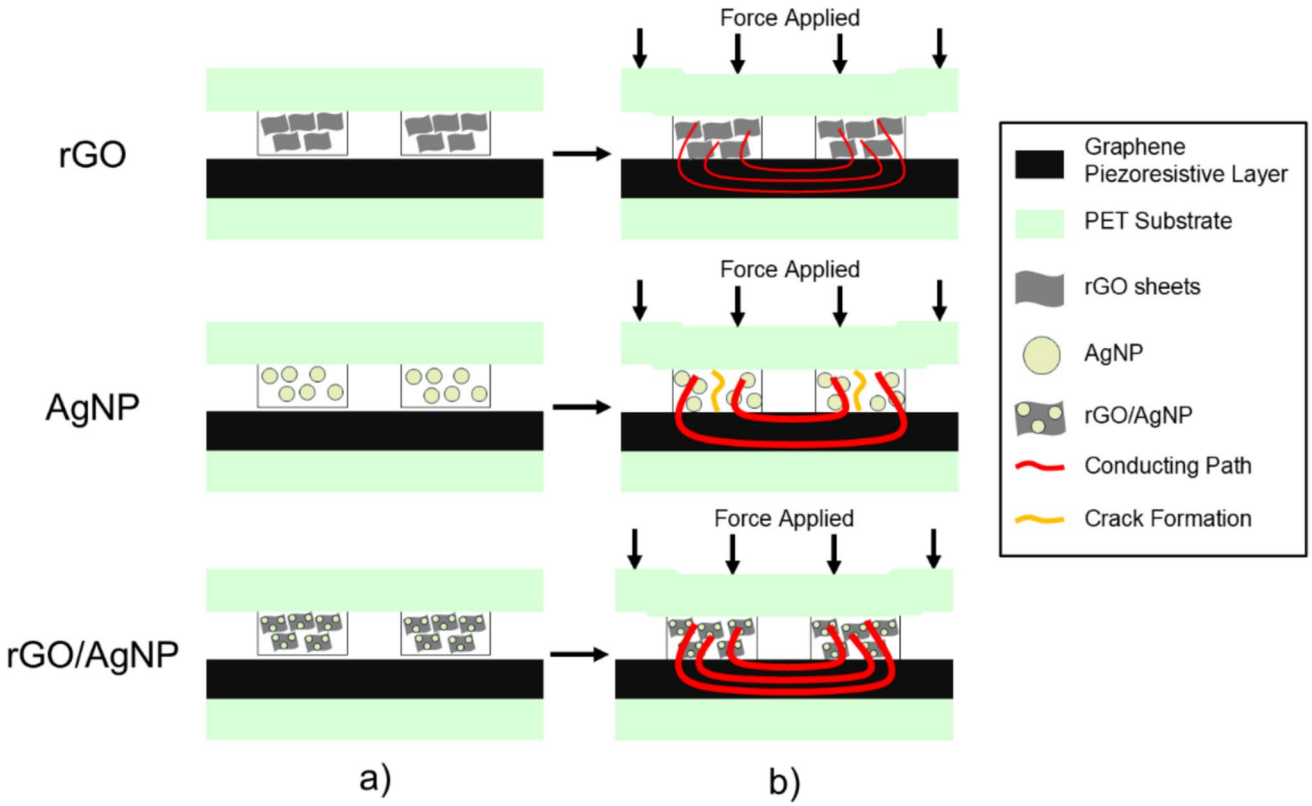

Fig. 12 Schematic illustration of sensing mechanisms using rGO sheets, AgNPs, and rGO/AgNP nanocomposite. **a** Initial state and **b** Pressed state

gap spacer in shunt mode configuration. The characterization results using the digital microscope show that the formulated ink is adhering to the substrate with a low percentage of error and can be printed onto the PET substrate. The developed sensor exhibits performance comparable to previously reported resistive tactile sensors, highlighting the effectiveness of the proposed rGO/AgNP nanocomposite electrode system and hybrid printing based fabrication strategy for low-force wearable sensing applications. This study primarily establishes the material formulation, device architecture, and baseline electromechanical performance, including sensitivity, dynamic response, and cyclic stability. Further work will focus on a more comprehensive characterization of the wearable sensing performance, including hysteresis behavior, environmental stability under temperature and humidity variations, and frequency-dependent response under operational conditions relevant to wearable use. In addition, future studies will aim to extend the sensing range beyond the current low-force regime through structural and material optimisation, enabling broader applicability in wearable and human–motion monitoring systems.

Table 1 Comparative analysis of previously fabricated sensors

Materials	Fabrication techniques	Performance parameter	Sensing range	Stability	Response and recovery time	Application	Remarks	References
• Substrate for electrode layer: Evolon PET and PA nonwoven fabric • Electrode layer: Liquid X printed metal MOD silver ink	• Electrode layer: Inkjet printing using Fujifilm Dimatix DMP-2850	R/R0 ≈ 10^{-6}	4.9 kPa–7.1 MPa	1000 cycles	• Response time: ~0.1 s • Recovery time: ~0.1 s	Detecting eyedropper bottle volume for glaucoma patients	Sharp drop in resistance after reaching threshold pressure	[36]
• Substrate for electrode: PET sheet • Electrode layer: EDAG 725-A Silver Flakes Ink • Substrate for active layer: PET sheet • Active layer: Loctite NCI-7002 (70%), Loctite ECI 7004-LR	• Electrode layer: Screen printing using screen mesh (100 threads per cm, 40 µm thick) • Active layer: Screen printing using screen mesh (100 threads per cm, 60 µm thick)	Decreases marginally at 20 N	1.0 N–100 N	10,000 cycles with 8% deviation	• Response time: 37.6 ms • Recovery time: 44.6 ms	Monitoring pressure distribution in wheelchair	High force range	[35]
• Substrate for electrode layer: Kapton polyimide film • Electrode layer: Metalon® HPS-FG32 silver screen ink • Substrate for active layer: Kapton polyimide film • Active Layer: MWCNT-TPU ink (5 wt% MWCNT weight percentage)	• Electrode layer: Screen printing using stainless steel screen mesh with 45° angle of attack, and 60–70 mm/s ink speed • Active layer: Screen printing using stainless steel screen mesh with 45° angle of attack, and 60–70 mm/s ink speed	0.528 V/N–15.1 V/N	0.04 N–1.3 N	60 cycles	• Response time: 70 ± 51 ms	Surgical magnetic microgripper	• Low force range • Low stability	[12]

Table 1 continued

Materials	Fabrication techniques	Performance parameter	Sensing range	Stability	Response and recovery time	Application	Remarks	References
• Substrate for electrode layer: DuPont Teonex PEN foil, 125 µm thickness (silver electrode), PVC foil, 80 µm thickness (gold electrode) • Electrode layer: UT Dots AGNP ink (silver electrode), unspecified gold leaf with 10 µm (gold electrode) • Substrate for active layer: GTS polyimide film • Active layer: Unspecified carbon ink	• Electrode layer: Inkjet printing using Fujifilm Dimatix DMP-2831 (silver electrode), Xurography using CE600-60 Plus cutting plotter (Gold Electrode) • Active layer: Gravure printing using RK printing proofer	8.56 Ω/N (silver electrode), 2.23 Ω/N (gold electrode)	0 N–100 N	Not reported	Not reported	Bite force measurement	High force range	[52]

Table 1 continued

Materials	Fabrication techniques	Performance parameter	Sensing range	Stability	Response and recovery time	Application	Remarks	References
• Substrate for electrode layer: PET sheet • Electrode layer: Formulated rGO/AgNP nanocomposite ink • Substrate for piezoresistive layer: PET sheet • Piezoresistive layer: rGO nanocomposite ink (Mi-Graphink)	• Electrode layer: Inkjet printing using Suss MicroTec LP50 printer • Piezoresistive layer: stencil printing directly onto substrate using squeegee	Fractional change of resistance of 0.35 and reaching saturated resistance at 35 kPa	Up to 35 kPa	400 cycles	• Response time: 164.0 ms • Recovery time: 161.54 ms	Wearable electronics	Continuous change of resistance during applied force • Optimum force range for application • High stability	This work

Acknowledgments

The authors would like to thank MIMOS Berhad and VLSI-MEMS Research unit, Kulliyyah of Engineering, International Islamic University Malaysia for providing laboratory facilities and technical support for this research. This work was supported by the Fundamental Research Grant Scheme (FRGS) research project FRGS24-341-0950 (FRGS/1/2024/TK07/UIAM/03/1).

Author contributions

The authors have contributed in such a way as follows: Muhammad Izzuddin Mohamad Azhar: Writing—original draft, material preparation, data collection and analysis. Aliza Aini Md Ralib: Conceptualization, data analysis, and validation, writing, review and editing. Nor Hidayati Diyana Nordin: Funding for the research, review and editing. Syed Muhammad Hafiz Syed Mohd Jaafar: Writing, data analysis, review and editing. Shafarina Azlinda Ahmad Kamal: Material preparation, review and editing. Nurul Hazierah Kamaruddin and Aiman Sajidah Abd Aziz: Data collection, review and editing. Aiman Sajidah Abd Aziz: Review and editing.

Funding

This work was supported by the Fundamental Research Grant Scheme (FRGS) research project FRGS24-341-0950 (FRGS/1/2024/TK07/UIAM/03/1).

Data availability

The data that support the findings of this study are available from the corresponding author upon reasonable request.

Declarations

Conflict of interest The authors declare that they have no known competing financial interests or personal relationships that could have appeared to influence the work reported in this paper.

Supplementary Information The online version contains supplementary material available at https://doi.org/10.1007/s10854-026-17553-w.

References

1. Q. Shu et al., Flexible resistive tactile pressure sensors. J. Mater. Chem. A (2024). https://doi.org/10.1039/d3ta06976a
2. K.Y. Shin, J.S. Lee, J. Jang, Highly sensitive, wearable and wireless pressure sensor using free-standing ZnO nanoneedle/PVDF hybrid thin film for heart rate monitoring. Nano Energy **22**, 95–104 (2016). https://doi.org/10.1016/j.nanoen.2016.02.012
3. T.P. Huynh, H. Haick, Autonomous flexible sensors for health monitoring. Adv. Mater. (2018). https://doi.org/10.1002/adma.201802337
4. Y. Gao, L. Yu, J.C. Yeo, C.T. Lim, Flexible hybrid sensors for health monitoring: materials and mechanisms to render wearability. Adv. Mater. (2020). https://doi.org/10.1002/adma.201902133
5. P. Roberts, M. Zadan, C. Majidi, Soft tactile sensing skins for robotics. Curr. Robot. Rep. **2**(3), 343–354 (2021). https://doi.org/10.1007/s43154-021-00065-2
6. C. Hegde, J. Su, J.M.R. Tan, K. He, X. Chen, S. Magdassi, Sensing in soft robotics. ACS Nano (2023). https://doi.org/10.1021/acsnano.3c04089
7. B. Shih et al., Design considerations for 3D printed, soft, multimaterial resistive sensors for soft robotics. Frontiers Robotics AI (2019). https://doi.org/10.3389/frobt.2019.00030
8. Y. Lian, H. Yu, M. Wang, X. Yang, H. Zhang, Ultrasensitive wearable pressure sensors based on silver nanowire-coated fabrics. Nanoscale Res. Lett. (2020). https://doi.org/10.1186/s11671-020-03303-2
9. Y. Hou, Z. Wang, H. Liu, M. Xia, X. Fan, Q. Ye, Designing a smart garment for dynamic sitting reminders. Sens. (2025). https://doi.org/10.3390/s25113359
10. D. Zhang, T. Huang, L. Duan, Emerging self-emissive technologies for flexible displays. Adv. Mater. (2020). https://doi.org/10.1002/adma.201902391
11. H. Yang et al., Ag-Grid and Ag-Nanowires hybrid transparent electrodes to improve performance of flexible organic light-emitting devices. Photonics (2025). https://doi.org/10.3390/photonics12030272
12. D.A. Aubeeluck, C. Forbrigger, S.M. Taromsari, T. Chen, E. Diller, H.E. Naguib, Screen-printed resistive tactile sensor for monitoring tissue interaction forces on a surgical magnetic microgripper. **15**, 28 (2023)
13. H. Niu, S. Gao, W. Yue, Y. Li, W. Zhou, H. Liu, Highly morphology-controllable and highly sensitive capacitive tactile sensor based on epidermis-dermis-inspired interlocked asymmetric-nanocone arrays for detection of tiny pressure. Small (2020). https://doi.org/10.1002/smll.201904774
14. N.A. Ramli, A.N. Nordin, N. Zainul Azlan, Development of low cost screen-printed piezoresistive strain sensor for facial expressions recognition systems. Microelectron. Eng. **234**, 111440 (2020). https://doi.org/10.1016/j.mee.2020.111440
15. J. Shintake, E. Piskarev, S.H. Jeong, D. Floreano, Ultrastretchable strain sensors using carbon black-filled elastomer composites and comparison of capacitive versus resistive sensors. Adv. Mater. Technol. **3**(3), 1–8 (2018). https://doi.org/10.1002/admt.201700284
16. J. Kerminen, J. Wiklund, A. Karakoç, K. Ruttik, R. Jäntti, H. Yiğitler, Characterization of low-cost inkjet printed-photonic cured strain gauges for remote sensing and structural monitoring applications. **7**(4), 647–660 (2021)
17. C. Zlebic, L. Zivanov, A. Menicanin, N. Blaz, M. Damnjanovic, Inkjet printed resistive strain gages on flexible substrates. Facta Univ. Ser. Electron. Energet. **29**(1), 89–100 (2016). https://doi.org/10.2298/fuee1601089z
18. J. He et al., Recent advances of wearable and flexible piezoresistivity pressure sensor devices and its future prospects. J. Materiom. **6**(1), 86–101 (2020). https://doi.org/10.1016/j.jmat.2020.01.009
19. P.N. Gunaratne, H. Tamura, An EMG-based GRU model for estimating foot pressure to support active ankle orthosis development. Sens. (2025). https://doi.org/10.3390/s25113558
20. F.A. Cholico et al., Comparing the pressure on the carpal tunnel when using an ergonomic pointer driver and an optical alternative. J. Funct. Morphol. Kinesiol. (2024). https://doi.org/10.3390/jfmk9040260
21. L. Kogan, T.L. Weadon, T. Evans, D.B. DeVallance, E.M. Sabolsky, Testing of tactile sensors for space applications, in Sensors and Smart Structures Technologies for Civil, Mechanical, and Aerospace Systems 2015. SPIE (2015). https://doi.org/10.1117/12.2085576
22. H. Jahanshahi, Z.H. Zhu, A comprehensive review of tactile sensing technologies in space robotics. Elsevier B.V. **38**(7), 103423 (2025). https://doi.org/10.1016/j.cja.2025.103423
23. Y. Shi, G. Shen, Haptic sensing and feedback techniques toward virtual reality. Res. (2024). https://doi.org/10.34133/research.0333

24. T. Chen et al., Novel augmented reality interface using a self-powered triboelectric based virtual reality 3D-control sensor. Nano Energy **51**, 162–172 (2018). https://doi.org/10.1016/j.nanoen.2018.06.022
25. L. Duan, D.R. D'hooge, L. Cardon, Recent progress on flexible and stretchable piezoresistive strain sensors: from design to application. Prog. Mater. Sci. **114**, 100617 (2020). https://doi.org/10.1016/j.pmatsci.2019.100617
26. M. Cheng et al., A review of flexible force sensors for human health monitoring. J. Adv. Res. **26**, 53–68 (2020). https://doi.org/10.1016/j.jare.2020.07.001
27. Y. Huang, X. Fan, S.C. Chen, N. Zhao, Emerging technologies of flexible pressure sensors: materials, modeling, devices, and manufacturing. Adv. Funct. Mater. **29**(12), 1–24 (2019). https://doi.org/10.1002/adfm.201808509
28. M.Y. Liu et al., Advance on flexible pressure sensors based on metal and carbonaceous nanomaterial. Nano Energy **87**(May), 106181 (2021). https://doi.org/10.1016/j.nanoen.2021.106181
29. U.P. Claver, G. Zhao, Recent progress in flexible pressure sensors based electronic skin. Adv. Eng. Mater. **23**(5), 1–17 (2021). https://doi.org/10.1002/adem.202001187
30. K.S. Kumar, P.-Y. Chen, H. Ren, A review of printable flexible and stretchable tactile sensors. Res. (2019). https://doi.org/10.34133/2019/3018568
31. N.A.C. Mustapha, A.H.M.Z. Alam, S. Khan, A.W. Azman, Parasitic consideration for differential capacitive sensor. Bull. Electr. Eng. Inform. **8**(3), 798–807 (2019). https://doi.org/10.11591/eei.v8i3.1526
32. K. Dai et al., Simulation and structure optimization of triboelectric nanogenerators considering the effects of parasitic capacitance. Nano Res. **10**(1), 157–171 (2017). https://doi.org/10.1007/s12274-016-1275-7
33. Y. Duan, S. He, J. Wu, B. Su, Y. Wang, Recent progress in flexible pressure sensor arrays. Nanomater. (2022). https://doi.org/10.3390/nano12142495
34. L. Chen et al., Flexible piezoresistive sensor based on CNT/PVA composite with wide linear detection range for human motion monitoring. Polym. (2025). https://doi.org/10.3390/polym17101378
35. J. Ahmad, H. Andersson, J. Sidén, Screen-printed piezoresistive sensors for monitoring pressure distribution in wheelchair. IEEE Sens. J. **19**(6), 2055–2063 (2019). https://doi.org/10.1109/JSEN.2018.2885638
36. B. Ju et al., Inkjet printed textile force sensitive resistors for wearable and healthcare devices. Adv. Healthc. Mater. (2021). https://doi.org/10.1002/adhm.202100893
37. D. Gräbner, M. Tintelott, K. Schön, W. Lang, Screen-printed resistive pressure sensors: influence of electrode geometry on the performance and on cross-sensitivity to strain and temperature", in *Journal of Physics: Conference Series*. IOP Publ. Ltd (2021). https://doi.org/10.1088/1742-6596/1837/1/012004
38. V. Allam, S.K. Vandrangi, Carbon black and boron nitride conductive fillers dispersed porous conductive polymer composite-based piezoresistive sensor for biomedical applications. J. Mater. Sci. Mater. Electron. (2024). https://doi.org/10.1007/s10854-024-14020-2
39. A.V. Tran, X. Zhang, B. Zhu, Mechanical structural design of a piezoresistive pressure sensor for low-pressure measurement: a computational analysis by increases in the sensor sensitivity. Sens. (2018). https://doi.org/10.3390/s18072023
40. X. Liu, M. Mwangi, X. Li, M. O'Brien, G.M. Whitesides, Paper-based piezoresistive MEMS sensors. Lab Chip **11**(13), 2189–2196 (2011). https://doi.org/10.1039/c1lc20161a
41. Z.G. Xiao, C. Menon, A review of force myography research and development. Sens. (2019). https://doi.org/10.3390/s19204557
42. O. Sherif, M.M. Bassuoni, O. Mehrez, A survey on the state of the art of force myography technique (FMG): analysis and assessment. Med. Biol. Eng. Comput. (2024). https://doi.org/10.1007/s11517-024-03019-w
43. X. Guo et al., Bioinspired low hysteresis flexible pressure sensor using nanocomposites of Multiwalled Carbon Nanotubes, Silicone Rubber, and Carbon Nanofiber for Human-Computer Interaction. ACS Appl. Nano Mater. **7**(13), 15626–15639 (2024). https://doi.org/10.1021/acsanm.4c02631
44. Y. Zhao et al., A high-sensitivity, fast-response sawtooth-structured flexible pressure sensor based on MWCNTs/rubber composites for machine learning-assisted recognition. ACS Appl. Polym. Mater. **7**(12), 8022–8033 (2025). https://doi.org/10.1021/acsapm.5c01069
45. J. Park et al., Giant tunneling piezoresistance of composite elastomers with interlocked microdome arrays for ultrasensitive and multimodal electronic skins. ACS Nano **8**(5), 4689–4697 (2014). https://doi.org/10.1021/nn500441k
46. X. Guo et al., Tactile corpuscle-inspired piezoresistive sensors based on (3-aminopropyl) triethoxysilane-enhanced CNPs/carboxylated MWCNTs/cellulosic fiber composites for textile electronics. J. Colloid Interface Sci. **660**, 203–214 (2024). https://doi.org/10.1016/j.jcis.2024.01.059
47. Y. Lu, T. Lei, Y. Qin, X. Wang, A flexible pressure sensor based on embedded cracks and stiffness-regulating layer with high detection limits and wide test ranges. J. Mater. Sci. Mater. Electron. (2024). https://doi.org/10.1007/s10854-023-11835-3

48. R. Tang et al., Flexible pressure sensors with microstructures. Nano Select **2**(10), 1874–1901 (2021). https://doi.org/10.1002/nano.202100003
49. M. Nabeel, M. Mousa, B. Viskolcz, B. Fiser, L. Vanyorek, Recent advances in flexible foam pressure sensors: manufacturing, characterization, and applications–a review. Polym. Rev. (2024). https://doi.org/10.1080/15583724.2023.2262558
50. C. Liu et al., 3D printing technologies for flexible tactile sensors toward wearable electronics and electronic skin. Polym. (Basel) **10**(6), 1–31 (2018). https://doi.org/10.3390/polym10060629
51. D. Vasiljević, D. Brajković, D. Krklješ, B. Obrenović, G.M. Stojanović, Testing and characterization of multilayer force sensing resistors fabricated on flexible substrate. Inf. MIDEM **47**(1), 40–48 (2017)
52. G. Stojanović et al., Comparison of performances of flexible tailor-made force sensing resistors fabricated using Inkjet and Xurographic techniques. J. Sens. (2019). https://doi.org/10.1155/2019/9181492
53. R. Søndergaard, M. Hösel, D. Angmo, T.T. Larsen-Olsen, F.C. Krebs, Roll-to-roll fabrication of polymer solar cells open access under CC BY-NC-ND license. **155**, 36–49 (2012)
54. H.W. Tan, T. Tran, C.K. Chua, A review of printed passive electronic components through fully additive manufacturing methods. Virtual Phys. Prototyp. (2016). https://doi.org/10.1080/17452759.2016.1217586
55. P. Martins et al., Advances in printing and electronics: from engagement to commitment. Adv. Funct. Mater. (2023). https://doi.org/10.1002/adfm.202213744
56. J. Wiklund et al., A review on printed electronics: fabrication methods, inks, substrates, applications and environmental impacts. J. Manuf. Mater. Process. (2021). https://doi.org/10.3390/jmmp5030089
57. K.-S. Kwon, Md.K. Rahman, T.H. Phung, S. Hoath, S. Jeong, J.S. Kim, Review of digital printing technologies for electronic materials. Flexi. Print. Electron. (2020). https://doi.org/10.1088/2058-8585/abc8ca
58. S.M.F. Cruz, L.A. Rocha, J.C. Viana, "Printing Technologies on Flexible Substrates for Printed Electronics", in *Flexible Electronics*. INTECH (2018). https://doi.org/10.5772/intechopen.76161
59. B. Derby, Inkjet printing of functional and structural materials: fluid property requirements, feature stability, and resolution. Annu. Rev. Mater. Res. **40**, 395–414 (2010). https://doi.org/10.1146/annurev-matsci-070909-104502
60. K. Weiß, H. Wörn, The Working Principle of Resistive Tactile Sensor Cells. IEEE. **1**(471), 476 (2005)
61. N.H. Ismail, N. Abdul Rashid, S.M.H. Syed Mohd Jaafar, S.F. Kamarudin, H.W. Lee, Electrical and mechanical performance of Inkjet-printed flexible electrodes based on reduced graphene oxide/silver nanoparticles. J. Mater. Sci. Mater. Electron. (2024). https://doi.org/10.1007/s10854-024-12273-5
62. N. N. Mohd Maidin *et al.*, 2023. Design, fabrication, and characterization of a graphene-based flexible electrode for in-vivo evaluation of wound healing in mice," in *2023 IEEE International Conference on Sensors and Nanotechnology, SENNANO 2023*, Institute of Electrical and Electronics Engineers Inc., 9 12. https://doi.org/10.1109/SENNANO57767.2023.10352542.
63. M. I. Mohamad Azhar *et al.*, 2025. Design and simulation of printed force sensitive resistor for wearable electronics," in *2025 10th International Conference on Computer and Communication Engineering (ICCCE)*, Institute of Electrical and Electronics Engineers Inc., 401 405. https://doi.org/10.1109/ICCCE66530.2025.11474027.
64. Y.Z.N. Htwe, I.N. Hidayah, M. Mariatti, Performance of inkjet-printed strain sensor based on graphene/silver nanoparticles hybrid conductive inks on polyvinyl alcohol substrate. J. Mater. Sci. Mater. Electron. **31**(18), 15361–15371 (2020). https://doi.org/10.1007/s10854-020-04100-4
65. Z.D. Chen et al., Reduced graphene oxide as saturable absorbers for erbium-doped passively mode-locked fiber laser. Chin. Phys. B (2018). https://doi.org/10.1088/1674-1056/27/8/084206
66. L. He, S.C. Tjong, Facile synthesis of silver-decorated reduced graphene oxide as a hybrid filler material for electrically conductive polymer composites. RSC Adv. **5**(20), 15070–15076 (2015). https://doi.org/10.1039/c5ra00257e
67. A. Albrecht et al., Over-stretching tolerant conductors on rubber films by inkjet-printing silver nanoparticles for wearables. Polym. (2018). https://doi.org/10.3390/POLYM10121413
68. M. Sarno, M. Casa, Green and one-step synthesis for Ag/graphene hybrid supercapacitor with remarkable performance. J. Phys. Chem. Solids **120**, 241–249 (2018). https://doi.org/10.1016/j.jpcs.2018.04.045
69. T. Liu et al., Inkjet printing high performance flexible electrodes via a graphene decorated Ag ink. Surf. Interfaces (2022). https://doi.org/10.1016/j.surfin.2021.101609
70. N. Neella, V. Gaddam, M. M. Nayak, N. S. Dinesh, K. Rajanna, Scalable fabrication of highly sensitive flexible temperature sensors based on silver nanoparticles coated reduced graphene oxide nanocomposite thin films. Sens. Actuators A Phys. **268**, 173–182 (2017). https://doi.org/10.1016/j.sna.2017.11.011

71. D.J. Van Den Heever, K. Schreve, C. Scheffer, Tactile sensing using force sensing resistors and a super-resolution algorithm. IEEE Sens. J. **9**(1), 29–35 (2009). https://doi.org/10.1109/JSEN.2008.2008891
72. M.M. Kellera, R.Y. Barnesa, M. Keller, B. Pretorius, Activities of daily living with grasp types and force measurements during object manipulation. S. Afr. J. Occup. Ther. **54**, 1 (2024)
73. K.N.M. Sobh, N.A.A. Razak, N.A.A. Osman, A FSR sensor cuff to measure muscle activation during strength and gait cycle for lower limb. IEEE. Access **10**, 106135–106147 (2022). https://doi.org/10.1109/ACCESS.2022.3207497